ADVANCED FUNCTIONAL MATERIALS
www.afm-journal.de

In-Plane Liquid Crystalline Texture of High-Performance Thienothiophene Copolymer Thin Films

By *Xinran Zhang, Steven D. Hudson,* Dean M. DeLongchamp,* David J. Gundlach, Martin Heeney,* and *Iain McCulloch*

Poly(2,5-Bis(3-alkylthiophen-2-yl)thieno[3,2-b]thiophenes (pBTTTs) are a new class of solution-processable polymer semiconductors with high charge carrier mobilities that rival amorphous silicon. This exceptional performance is thought to originate in the microstructure of pBTTT films, which exhibit high crystallinity and a surface topography of wide terraces. However, the true lateral grain size has not been determined, despite the critical impact grain boundaries can have on the charge transport of polymer semiconductors. Here a strategy for determining the lateral grain structure of pBTTT using dark-field transmission electron microscopy (DF-TEM) and subsequent image analysis is presented. For the first time, it is revealed that the in-plain pBTTT crystal orientation varies smoothly across a length scale significantly less than one micrometer (e.g., with only small angles between adjacent diffracting regions). The pBTTT polymers thus exhibit an in-plane liquid crystalline texture. This microstructure is different from what has been reported for small molecule semiconductors or polymer semiconductors such as poly (3-hexyl thiophene) (P3HT). Even though films processed differently exhibit different apparent domain sizes, they exhibit similar charge carrier hopping activation energies because they possess similar low densities of abrupt grain boundaries.

1. Introduction

Charge carrier transport[1] is a critical process in organic electronic devices, which use thin layers of flexible and solution-processable organic semiconductors as active materials.[2] The charge carrier mobility (μ) of an organic semiconductor strongly depends on the microstructure of the film[3] and μ can increase by orders of magnitude from amorphous to polycrystalline films. Intensive structural characterization of small molecules such as pentacene[4] and polymers such as poly (3-hexylthiophene) (P3HT)[5] has revealed that charge transport in polycrystalline films is affected primarily by two aspects of the microstructure: grain orientation,[1,3–5] and grain boundaries in the transport plane.[6] The orientation of crystal grains is important due to the inherent anisotropy of most rigid organic semiconducting molecules; transport is typically fast within a molecule and along packing directions with good π–π overlap, whereas transport is slower along packing directions with poor π–π overlap. Grain boundaries are regarded as highly resistive interruptions to charge transport.

Whole-film microstructure analysis techniques such as X-ray diffraction (XRD) or photon absorption spectroscopies are typically insensitive to grain boundaries, and a spatially-resolved orientation mapping technique is therefore required to correlate charge carrier mobility with microstructure. Although scanning probe techniques such as atomic force microscopy (AFM) are valuable for collecting images of surface topography, they are not intrinsically sensitive to grain boundaries or grain orientation except in special modes such as transverse shear microscopy,[7] which has been demonstrated on pentacene but not on polymers. Dark-field (DF) transmission electron microscopy (TEM) is an attractive candidate technique that can be applied to both small molecule and polymer semiconductor films because it combines aspects of grain orientation measurement and grain boundary identification with a high spatial resolution imaging capability.

Here we apply DF-TEM to measure the microstructure of poly(2,5-Bis(3-alkylthiophen-2-yl)thieno[3,2-b] thiophene (pBTTT),[8] which is a class of state-of-the-art solution-processable semiconducting polymer with field-effect hole mobility as high as ~1 $cm^2 V^{-1} s^{-1}$ in optimized devices.[8a,8c] The pBTTT polymers are an important target for spatially-resolved grain measurements because they appear highly crystalline in XRD, and in AFM they exhibit wide terraces that appear to extend laterally several hundreds of nanometers.[8b,8e] Accurate determination of lateral grain size, however, has not been possible by these techniques because large areas of common

[*] Dr. X. Zhang, Dr. S. D. Hudson, Dr. D. M. DeLongchamp
Polymers Division
Materials Science and Engineering Laboratory
National Institute of Standards and Technology
Gaithersburg, MD 20899, USA
E-mail: sdh@nist.gov; deand@nist.gov
Dr. D. J. Gundlach
Semiconductor Electronics Division
Electronics and Electrical Engineering Laboratory
National Institute of Standards and Technology
Gaithersburg, MD 20899, USA
Prof. M. Heeney, Prof. I. McCulloch
Department of Chemistry
Imperial College London
South Kensington, SW7 2AZ, UK

DOI: 10.1002/adfm.201001232

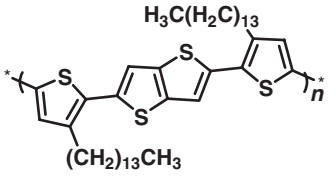

Scheme 1. Chemical structure of pBTTT-C_{14}.

height do not necessarily require a single crystalline domain, nor do steps necessarily indicate a change in crystal orientation. Without grain size measurements, it is not possible to determine how lateral film microstructure affects the charge carrier mobility of pBTTT, or whether that microstructure can be improved by altering the pBTTT processing. In this work, we performed DF-TEM on two films of a pBTTT with tetradecyl side chains (pBTTT-C_{14}, **Scheme 1**) that were processed differently to create different terrace sizes as observed by AFM. Larger terraces appear on an annealed pBTTT-C_{14} film (~25 nm thick) cast from a 4 mg mL^{-1} solution in a solvent pair of 1:8 *o*-dichlorobenzene to chloroform by volume (that film hereafter referred to as SP), whereas smaller terraces appeared on an annealed pBTTT-C_{14} film (~15 nm thick) cast from a 5 mg mL^{-1} solution in pure 1,2,4-trichlorobenzene (that film hereafter referred to as TCB). Both films were subjected to the same thermal annealing procedure (180 °C for 5 min). In both films, the size of a region within which the polymer chains are similarly oriented (such a region is referred to hereafter as a quasi-domain, since it is somewhat different from the conventional concept of a crystalline domain) was evaluated and directly correlated with charge carrier hopping activation energy extracted from variable-temperature charge-carrier-mobility measurements.

2. Results and Discussion

2.1. Electron Diffraction and Dark-Field TEM Imaging

The development of our DF-TEM imaging approach begins with selected-area electron diffraction (SAED), which provides the in-plane diffraction pattern and an approximation of the quasi-domain size. When the selected area is relatively large (e.g., several micrometers), concentric rings compose the diffraction pattern (**Figure 1a**). These rings are 00l and 0k0 reflections, representing spacings along the polymer backbone and the π–π stacking direction, respectively.[8b,8d,e] The 010 is the most intense reflection because π–π stacking represents the most substantial correlations between molecular subunits. The absence of h00 reflections indicates that this stacking direction is approximately normal to the substrate plane.

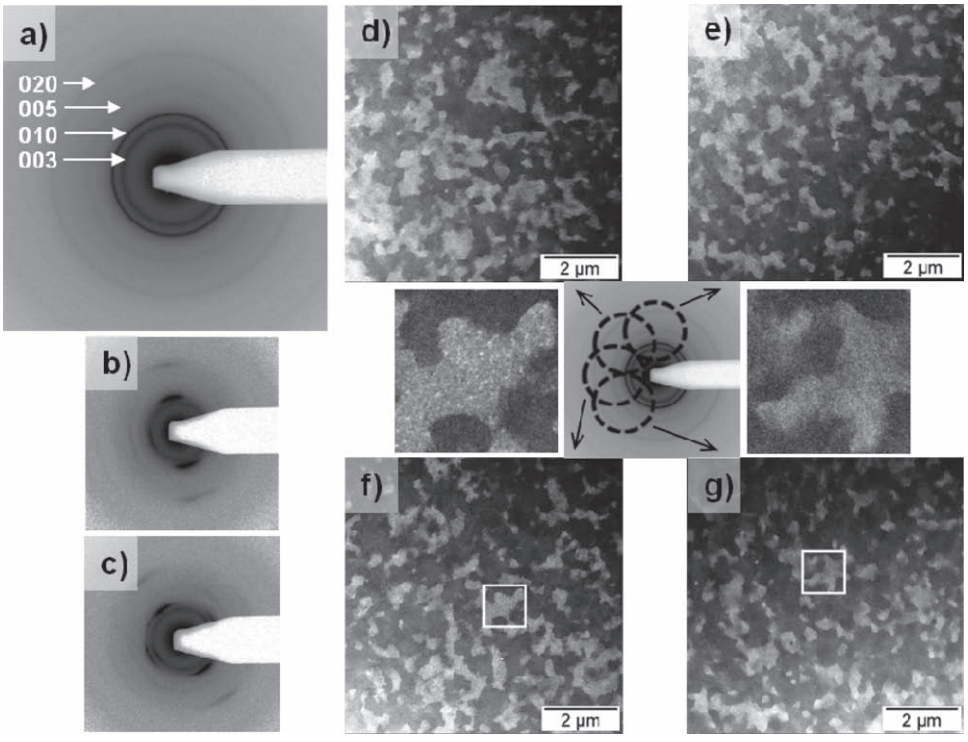

Figure 1. Diffraction patterns and dark-field TEM images acquired from an annealed pBTTT-C_{14} thin film (~25 nm thick) cast from a solvent pair of 1:8 *o*-dichlorobenzene to chloroform by volume: a) diffraction pattern from an area ~8 μm in diameter; b,c) diffraction patterns from areas ~250 nm in diameter; d–g) dark-field images with different beam-tilt configurations, as illustrated on the diffraction pattern (center inset). Shown is the position of objective aperture (actually stationary, see text) relative to the diffraction pattern. Squares cropped from (f) and (g) are magnified to show details within the crystalline quasi-domains. Note that the aperture locations are not absolute due to an arbitrary rotation of the field of view under magnification, but the relative rotations of the aperture about the center of the pattern are maintained.

This crystal orientation is consistent with analysis from grazing-incidence XRD which indicates that the [h00] vector is highly oriented about substrate normal in annealed pBTTT films.[8f] Since the SAED pattern shown in Figure 1a is composed of uniformly intense rings and not spots, the pBTTT-C_{14} must have randomly azimuthally oriented quasi-domains with a lateral size significantly smaller than 8 μm. When the beam size is reduced to ~250 nm, however, whole rings are no longer observed. Instead, a pair (Figure 1b) or pairs (Figure 1c) of smooth arcs (i.e., not spots) appear, suggesting that the quasi-domain size is comparable to ~250 nm, with numerous smaller crystals that lie within the beam spot having similar but finely distributed orientations. Here, we also note that the single diffuse orientation as shown in Figure 1c suggests a common orientation locally shared by vertically adjacent pBTTT molecular layers, contrary to what has been observed in some small molecule organic semiconductors.[7a] Multiple orientations through the film thickness are not readily observed, as evidenced by the results of specimen translation relative to the beam: the peak orientation either rotated, or a new one grew in intensity at the expense of the other as shown in Figure 1c. In such cases, it is relatively straightforward to map the in-plane crystal orientation, since any location on the film is represented by a single orientation.

DF-TEM images provide contrast based on the orientation of in-plane diffraction peaks, the brightest and most significant of which is the 010 for pBTTT. Dark field images were collected by tilting the beam such that only a specific arc of the 010 ring could pass through a centered objective aperture.[9] The image created on the image plane of the objective lens was therefore brightest for the quasi-domains that were oriented so that their diffraction spots could pass through the aperture. The beam tilt was adjusted away from the sample surface normal such that the 30 μm aperture should admit a range of the 010 ring encompassing an arc of ~90°, though we later discovered that the admitted arc was somewhat smaller. Although smaller apertures could have been used, much smaller apertures are impractical because to completely map the azimuthal orientations correspondingly more DF images would be required. Unfortunately, the limited critical dose for beam damage prevents the acquisition of more than ~8 images at our collection conditions. DF-TEM images (Figure 1d–g) were collected with a 45° increment of beam tilt azimuthal rotation. They exhibit high-contrast micrometer- or sub-micrometer-sized regions of common orientation (e.g., bright for those oriented within the admitted ~90° arc and dark for those not oriented within it). Furthermore, these crystalline quasi-domains all show signs of containing nanocrystals of tens of nanometers in diameter (see the speckled appearance of the magnified square from Figure 1f as well as of a DF image acquired at higher magnification shown in Figure S1 of the Supporting Information). This image is consistent with the diffraction patterns from small areas (Figure 1b,c). The typical size of the speckles is ~20 nm which is smaller than that of a fully extended chain of pBTTT-C_{14} (~60 nm).[8g] The local distribution of crystal orientations within a quasi-domain means that detection of such quasi-domains is much less sensitive to sample tilt,[10] facilitating quantitative analysis. In comparison, the commonly used bright-field (BF) imaging could not provide marked contrast (Figure S1) from the pBTTT films themselves due to the lack of mass-thickness difference. The poor contrast in BF mode supports a simple interpretation of the DF images, because it demonstrates that the film thickness is nearly uniform (in agreement with AFM images) and that the scattering efficiency is also nearly uniform. Local differences in electron scattering arise primarily then from differences in azimuthal material orientation.

2.2. Image Analysis

There are factors, however, that complicate an accurate analysis of crystal orientation from the DF images shown in Figure 1. Firstly, for each image, there is a contribution from the 003 reflection (as illustrated in the approximate beam-tilt configurations in Figure 1), as well as the dominant 010 reflection. Since these two reflections represent spacings along orthogonal directions, one might observe the same crystals in two images collected from orthogonal beam tilt azimuths. We instead observe that the crystalline quasi-domains are essentially complementary in pairs of images collected for orthogonal beam tilt azimuths (i.e., comparing Figure 1d with Figure 1g, or Figure 1e with Figure 1f), proving that the lower intensity of the 003 reflection does not significantly complicate the DF image analysis. It remains true that the 003 reflection, other weaker reflections from crystals or non-crystalline regions,[11] and inelastic scattering should result in a significant background level in each DF image. Secondly, the crystalline structure degrades gradually under illumination.[12] While the speckles within the crystalline quasi-domains are clearly observed (the magnified square from Figure 1f) at low electron beam dose, they are blurred (the magnified square from Figure 1g) after being exposed multiple times. The overall intensity and contrast of the DF images consequently decrease with increased exposure time, but the quasi-domain boundaries in Figure 1g are still clear enough for image analysis. The continuation of image acquisition would finally lead to blurred quasi-domain boundaries and significant distortion of the film. This gradual degradation limits the number of DF images that could be used for image analysis, and also makes the signal and background levels unequal in different DF images. Thirdly, the original DF images suffer from shadowing, i.e., a gradient of background intensity parallel to the azimuthal direction of the beam tilt, associated primarily with inelastic electron scattering.[13] The shadowing direction varies from image to image due to different beam-tilt azimuth (Figure 1d–g), making a direct image analysis almost impossible. Finally, the objective aperture does not lie exactly in the back focal plane, so that the intensity of beams admitted at the edge of the aperture are not as intense as those through the center. In view of these complications, the DF images acquired from the same area are subjected to a two step processing, specifically 1) averaging two images produced by admitting diametrically opposite diffraction and 2) local histogram equalization (described in detail in Supporting Information), prior to image analysis as a means of normalization.

The strategy used to analyze the processed images (shown in Figure S3) is based on a pixel-by-pixel method that associates intensity patterns with crystal orientations. Specifically, sets of four pixels from the same locations of different images are

considered in turn. The averaged gray value of each set is used as a threshold to identify whether each of the four pixels is "bright" or "dark." The use of an average accounts for differences in local film thickness and background etc. For a certain set, if the pixels are bright for two adjacent beam-tilt azimuths, e.g., I and II, and dark for the other two (illustrated in **Figure 2a**), this location will be considered being occupied by a quasi-domain that contributes to the pair of diffraction arcs admitted in both I and II. Correspondingly, a color (e.g., red) is assigned to the orientation range represented by this pair of arcs. Likewise, three other patterns with two adjacent bright (or dark) spots are assigned with yellow, cyan, and violet colors, respectively. Ideally, if the beam tilt configurations relative to the objective aperture exactly followed those shown in Figure 2a, we would obtain a four-color orientation map without unassigned pixel after analyzing all pixels in Figure S3. However, due to the factors described in the preceding paragraph, the resulting four color map has only 56% of the pixels colored (Figure 2d), indicating that other intensity patterns should also be taken into consideration.

The primary cause of other intensity patterns are non-ideal beam-tilt/aperture configurations (Figure 2b,c), which collect diffraction arcs that deviate from 90°, giving rise to the admittance of small sectors of elevated intensity either once (Figure 2b) or three times (Figure 2c). The resultant intensity patterns are responsible for 19% and 12% of the pixels, respectively. This could occur for several potential reasons: the imperfect edge of the objective aperture (e.g., from not being exactly at the back focal plane), experimental error in calibrating the beam-tilt azimuth, diffraction from reflections other than the 010, and slight tilt of the sample or its planar texture. The schematic configuration in Figure 2b is more likely in actuality, since it would be responsible for a larger percentage of pixels, and the intensity admitted through the aperture decreases near its edge. Moreover, the corresponding colored pixels shown in Figure 2e appear grain-like while those in Figure 2f are boundary-like,

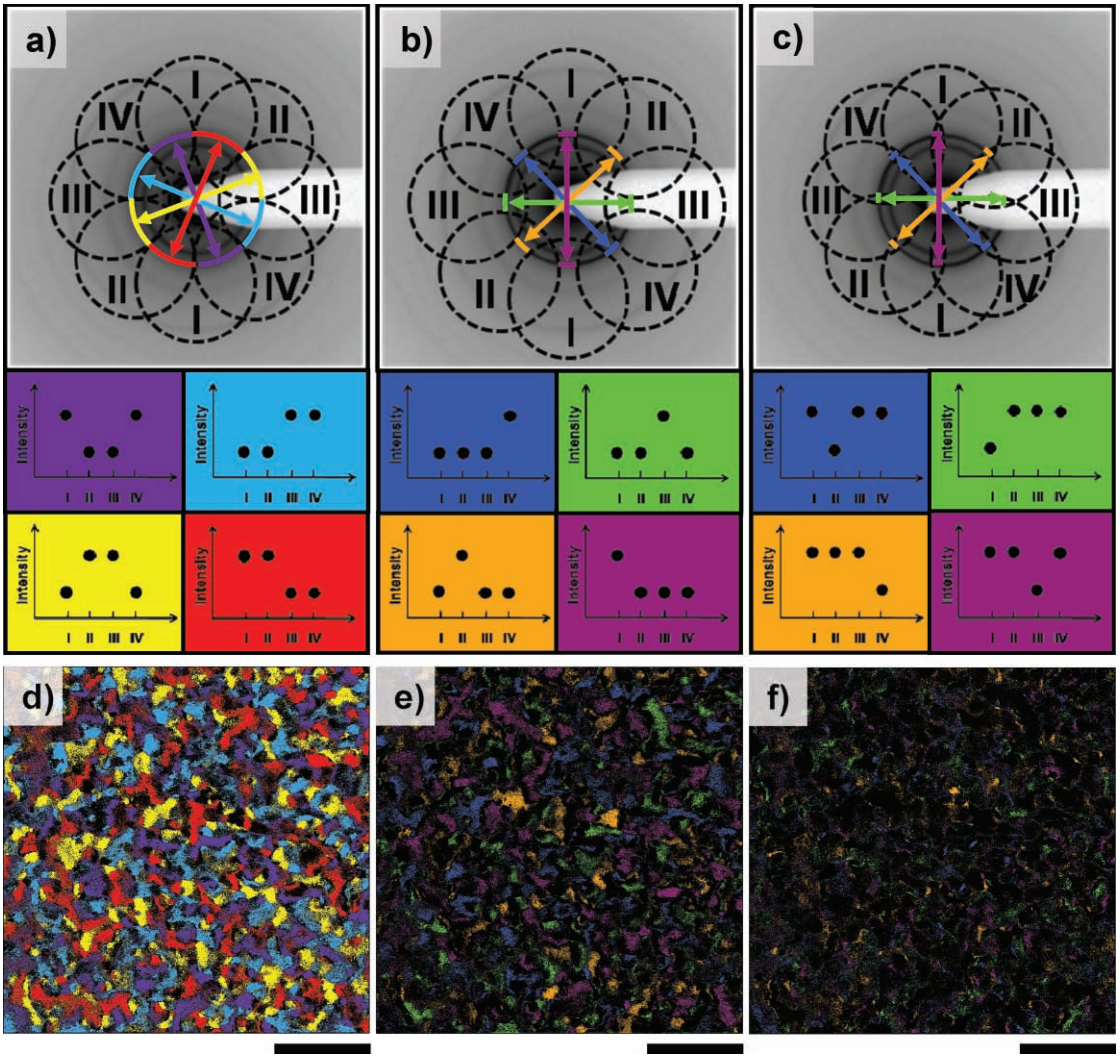

Figure 2. Illustration of the pixel-by-pixel image analysis: a) ideal and b,c) non-ideal beam tilt configurations, along with their resultant intensity patterns. Each pattern is assigned with a color which corresponds to certain orientation range represented by a pair of arcs; d–f) orientation maps resulted from a–c), respectively. The scale bars all denote 2 μm.

suggesting further that the intensity patterns associated with Figure 2b represent a well-defined orientation, while those of Figure 2c may represent mixed orientation that might be present at quasi-domain boundaries. We thus assign the intensity patterns shown in Figure 2b with colors (orange, green, blue and magenta) and leave those shown in Figure 2c unassigned. In this way, an eight-color orientation map is produced (**Figure 3a**, the combination of Figure 2d and Figure 2e) with the sectioned circle beside the map correlating each color with its corresponding crystal orientation range. The sectors are not equally weighted due to the different percentages of pixels (summarized in **Table 1**) they represent. Adjusting the sector width to match the relative percentages is consistent with the lack of in-plane texture. Note that there are still ~25% of unassigned (black) pixels corresponding to intensity patterns shown in Figure 2c and those with alternating high and low intensities (i.e., high intensities in I and III while low intensities in II and IV, or the reverse). Again, these might arise from the coexistence of multiple orientations within the range of a single pixel either laterally (boundary pixel) or vertically (stacking fault), or signal from the 003 reflection. However, the size, shape, and continuity of the colored quasi-domains are not significantly affected by the black pixels. Therefore, Figure 3a is an approximate but reasonable representation of the actual in-plane film microstructure.

2.3. In-Plane Microstructure of pBTTT-C_{14}

Figure 3a shows a notable liquid-crystal-like structure, i.e., it reveals a gradient transition of crystal orientations across the whole image range. Although quasi-domains with large orientation difference are sometimes found in direct contact (also implied by the diffraction pattern shown in Figure 1c), the boundaries are overwhelmingly low-angle (e.g., having an inter–quasi-domain angle equal or less than the resolution of this mapping strategy). This low angle transition is demonstrated quantitatively in Figure 3c (for minor colors) and Figure 3d (for major colors) which are generated from a simple neighborhood analysis of Figure 3a. As an example, among all the orange pixels in direct contact with different colored neighbors, 95% of them have red or yellow (denoted as R and Y, respectively, in the graph) nearest neighbors which are most similar to the orange pixels in terms of orientation (the orange curve in

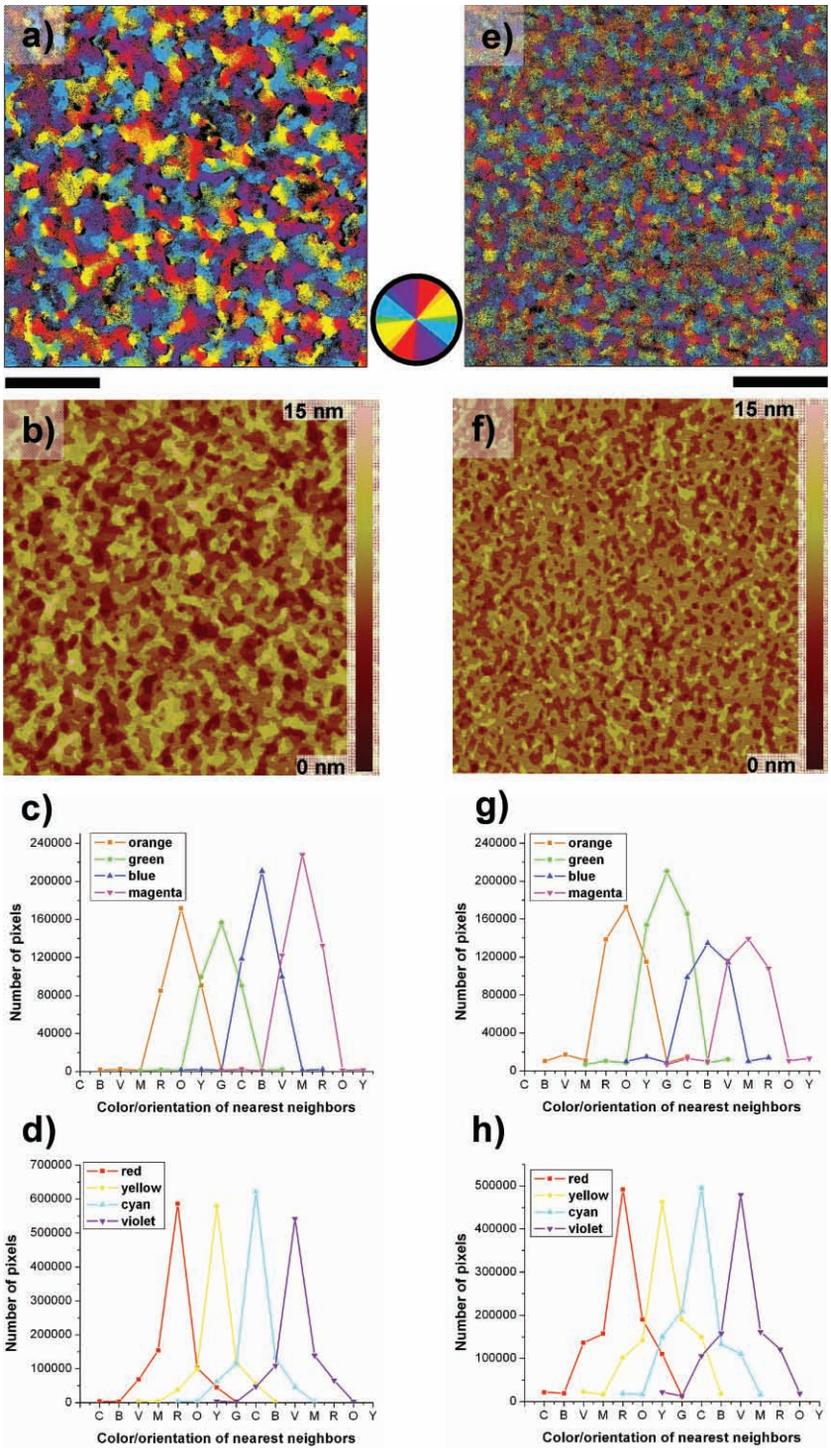

Figure 3. Orientation maps, AFM images and neighborhood analysis curves acquired from annealed SP film (~25 nm thick) and TCB film (~15 nm thick), respectively: a) and e) orientation maps obtained from the pixel-by-pixel analysis; b) and f) AFM images, the scale bars all denote 2 μm; c), d), g), and h) neighborhood analysis curves for all kinds of minor and major colored pixels. The line and symbol color corresponds to the kind of pixels being analyzed. Each curve shows the numbers of different colored pixels as the nearest neighbors of the kind of pixels being analyzed. The abbreviated names of the horizontal coordinates stand for red (R), orange (O), yellow (Y), green (G), cyan (C), blue (B), violet (V), and magenta (M), respectively.

Table 1. The distribution of colored pixels in terms of percentages of total pixel number in orientation maps obtained from the SP and TCB films, respectively.

Solvent	Red	Orange	Yellow	Green	Cyan	Blue	Violet	Magenta
SP	14%	4%	14%	4%	15%	5%	13%	6%
TCB	11%	4%	11%	6%	10%	5%	11%	4%

Figure 3c). For major colored pixels such as red ones, 68% are in contact with similarly oriented orange and magenta pixels. A considerable amount (30%) also have somewhat more misoriented yellow or violet nearest neighbors. The difference in statistics of neighbor orientation between major and minor colors likely results from the relative size of the orientation sectors they represent, consistent with a sample that has no preferred orientation or in-plane texture. It is reasonable to expect that most of the 30% red boundary pixels do not have a significant difference in crystal orientation compared with their yellow or violet neighbors. Since the orientation range represented by any kind of major colored pixels is relatively large (limited angle resolution), it is not clear whether the angle between adjacent nanocrystals could be smaller than that suggested by Figure 3c (i.e., >30°).

We address the issue of limited angle resolution with the tentative approach illustrated in Figure S4 (see Supporting Information). As shown by Figure S4a, another series of eight DF images were recorded from a different area of the SP film, with the beam tilt azimuthal rotation step of only ~10° instead of 45°. The image processing method for these images (described in the Supporting Information) is somewhat different from that for the previous DF images, due to the lack of images recorded by admitting diametrically opposing diffraction arcs. In spite of its unevenly weighted colors, the orientation map resulted from the pixel-by-pixel analysis again displays gradient transition of crystal orientations (Figure S4b), with a finer angle resolution compared with that of Figure 3 (~10°). In other words, Figure S4b suggests that the angle between adjacent pBTTT nanocrystals typically does not exceed 10°. Nevertheless, the unevenly weighted colors (Figure S4c–e) imply that the image analysis method needs to be improved when dealing with a much larger number of possible intensity patterns.

To quantify the quasi-domain size in Figure 3a, a 2D isotropic power spectrum was calculated (**Figure 4a**), and the characteristic length scale of this quasi-periodic structure was found to be ~950 nm. It was found that larger quasi-domain size could not be obtained by altering processing parameters such as solvent volatility and pBTTT concentration. The quasi-domain size is reduced when lower pBTTT concentration in the same solvent or similar pBTTT concentration in a less volatile solvent (such as *o*-dichlorobenzene or 1,2,4-trichlorobenzene) is used for spin-casting; in both cases the film thickness is also decreased. In this work, the largest difference in quasi-domain size observed by TEM was found between SP films (~25 nm thick) and TCB films (~15 nm thick). A crystal orientation map of the latter is shown in Figure 3e, with the processed DF images used for the pixel-by-pixel analysis shown in Figure S5 (see Supporting Information). The characteristic length scale extracted from 2D isotropic power spectrum of Figure 3e is ~600 nm (Figure 4b). Also shown in Figure 4 is the power spectra obtained from AFM images of the SP film and the TCB film. Interestingly, it appears that the quasi-domain size of a pBTTT-C_{14} film can be predicted by its AFM image, as an orientation map with smaller quasi-domain size (Figure 3e) corresponds

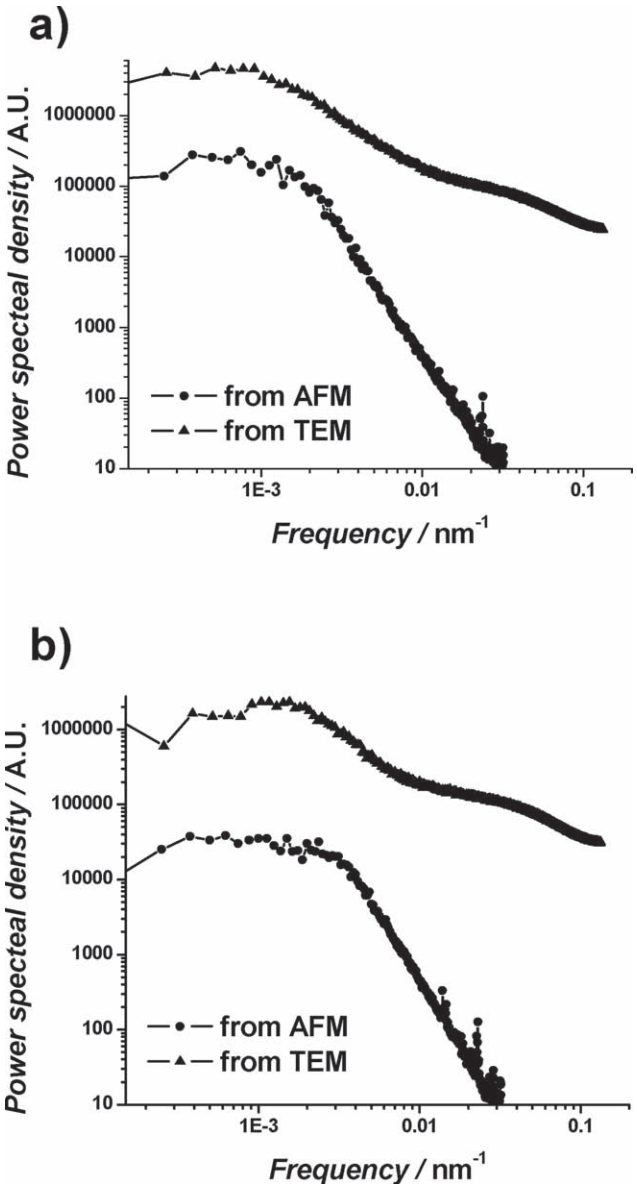

Figure 4. Power spectra calculated from orientation maps as well as AFM images: a) from the SP film (~25 nm thick); b) from the TCB film (~15 nm thick). The narrower spatial frequency range of those from the AFM images arises from their coarser resolution (15.6 nm per pixel) compared with that of the TEM images (3.8 nm per pixel).

to an AFM image with higher spatial frequencies (Figure 3f). However, any quantifiable correlation between the real grain structure and the terraced topography is still lacking. Compared with Figure 3a, there are fewer colored pixels in Figure 3e (Table 1). This result is consistent with our conjecture that some of the black pixels are boundary pixels where multiple quasi-domains with different orientations meet, since there should be more boundaries as the quasi-domain size decreases. The same neighborhood analysis was performed to Figure 3e, showing a similar trend that crystal orientation changes gradually across the TCB film.

Since such gradual changes in orientation suggest a texture similar to liquid crystals, we can search the map to determine whether it contains disclinations, and of what type. In our orientation maps such as Figure 3a, disclinations appear as points where the colors of the color wheel converge, i.e., quasi-domains of each orientation touching a common point. Integer disclinations would have each color appear twice (as in the color wheel) and for half-integer disclinations each color appears only once. Positive and negative disclinations are discriminated by tracking the sequence of colors around this point. To show the disclinations more clearly, a rectangle from the lower left part of Figure 3a is cropped and magnified **in Figure 5**. As seen from the encircled areas, all of the disclinations are of half-integer type and those of opposite sign are always found near one another, i.e., there are not clusters of positive or negative without their opposite, indicative of a liquid crystalline texture.[14] These disclinations of course represent regions of high curvature, which have also been observed in other rigid polymers.[15] We note that a smectic mesophase was identified for pBTTT in our previous work.[8e] The vertical layer order of pBTTT is established upon entering the mesophase through a transition at ~158 °C, and preserved by reinterdigitation of the side chains upon cooling.[8e] But the in-plane organization remained unknown. Here we are able to determine, for the first time, that the in-plane texture is nematic like.

Having determined that the order exhibited by these semicrystalline films bears resemblance to liquid crystal systems, we recall that DF-TEM was applied previously, to determine orientation patterns and textures of liquid crystalline polymers.[16a,b] In those cases, quantitative analysis was not attempted in detail and a semicrystalline lamellar decoration technique proved more convenient for a 2D mapping of orientation[16c] that did enable quantitative analysis.[16d,e] Although the present case is also semicrystalline polymer, the crystal shape is not lamellar and being isometric does not indicate the underlying molecular orientation.

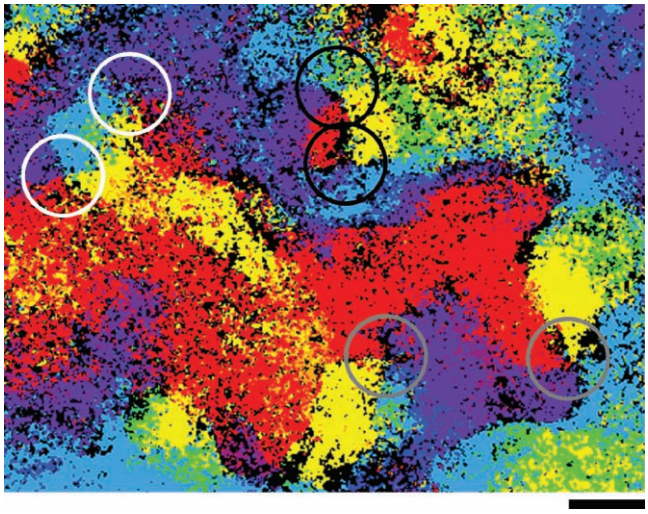

Figure 5. A cutout from Figure 3a with higher magnification, showing disclinations of half-integer type. Some of these are highlighted with circles, and a few others are also present. The pairing of the disclinations is indicated, for example by the white and black pairs of circles. For reference, the defect circled in gray at the right side of the figure is classified positive. The scale bar denotes 200 nm.

2.4. Correlation Between Quasi-Domain Size and Charge Transport Properties

Since the quasi-domain size is distinctly different between the two films mentioned above, it is interesting to compare their transistor performance, and thus evaluate the role of quasi-domain size in determining the electrical properties of pBTTT-C_{14} films. Bottom-contact bottom-gated transistors were made from both films. For all channel lengths used in our measurement (10 to 80) μm, the saturation hole mobility (μ_{sat}) at room temperature extracted from the transfer curves were found to be similar between these two films. We further subjected the films to variable temperature measurements. The μ_{sat}-$1/T$ plots shown in **Figure 6** suggest that the mobility for each film is thermally activated. The μ_{sat} values in these plots were obtained from devices with the longest channel length (80 μm) available in this study, as they should be the least affected by contact resistance. The activation energy (E_a) extracted from the slope of the linear fit is 55 meV for the SP film, and 58 meV for the TCB film. Thus, in spite of their ~30% difference in quasi-domain size, these two films actually have comparable field-effect charge transport properties.

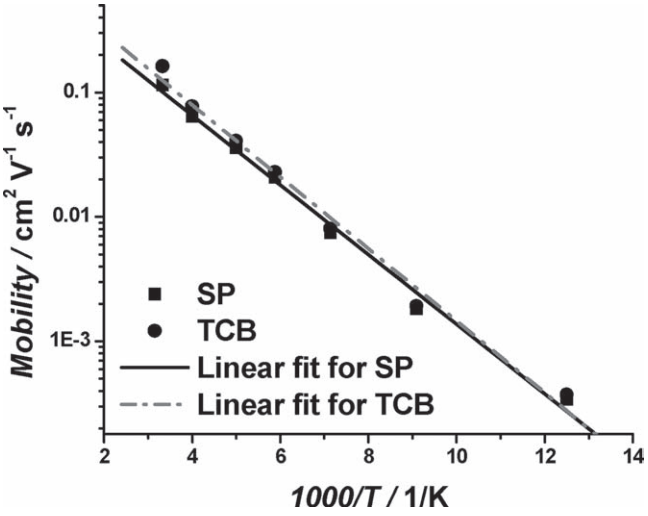

Figure 6. μ_{sat}-$1/T$ plots for the SP film (~25 nm) and the TCB film (~15 nm). Uncertainty for temperature measurement is ±1% and the fitting error for μ_{sat} is ±2%.

The correlation between the quasi-domain size and the charge transport properties shown above suggest that pBTTT thin films may not have numerous abrupt grain boundaries as are often thought to occur in organic semiconductors.[6a–d] Instead it may be viewed as a uniform distribution of defects that leads to small but continuous variance of molecular orientation. In other words, pBTTT molecules undergo large change of orientation over a relatively long range (multiple quasi-domains), while locally the quasi-domains resemble conventional liquid crystalline order. The boundaries between adjacent quasi-domains observed in Figure 3a and 3e are not absolute, as they are resulted from the beam-tilt configurations used in our measurement. They would change positions under a set of different beam-tilt configurations, and thus a boundary-containing region is basically the same with the interior of a quasi-domain. Although different processing conditions result in different apparent quasi-domain sizes (SP and TCB films), the actual difference is the length scale over which orientation varies. The reason this difference is not reflected in the electrical behavior may be because the low density of abrupt grain boundaries is not changed, so that both films can provide percolative pathways for charge transport that is limited by the local liquid crystalline orientation distribution.

3. Conclusions

DF-TEM reveals a liquid-crystal-like in-plane microstructure of spin-cast pBTTT-C_{14} films. The in-plane crystal orientation changes smoothly across the length scale of an organic thin-film transistor (OTFT) device. This structure leads to a relative insensitivity in OTFT device properties—such as μ_{sat} and E_a—to the quasi-domain size. Although quasi-domain size can be changed by processing, and appears most closely correlated to film thickness, there remains a similar low density of abrupt grain boundaries within the material in the OTFT channel. Even within quasi-domains, there is a modest distribution of crystal orientation that may ultimately dominate charge transport processes. The DF-TEM analysis technique demonstrated here shows significant promise in mapping the in-plane crystal orientation of crystalline polymer semiconductors. The resulting orientation maps reveal far more details about the lateral film microstructure of pBTTT-C_{14} thin films than AFM images typically do. Application of this technique across a wide range of polymer semiconductors should contribute to structure-property relationships that can guide future materials and process development efforts.

4. Experimental Section

Materials and Sample Preparation: The semiconducting polymer pBTTT-C_{14} was synthesized by using Stille coupling as reported previously.[17] Two kinds of thin films were made from pBTTT-C_{14} solutions of 4 mg mL^{-1} in a solvent pair of 1:8 *o*-dichlorobenzene to chloroform by volume or 5 mg mL^{-1} in pure 1,2,4-trichlorobenzene at 80 °C. Substrates were the native oxides of <100> silicon cleaned by ozone exposure for 10 min and then exposed to 0.002 M octyltrichlorosilane (Gelest) in anhydrous hexadecane (Aldrich)[18] for 16 h to result in a water contact angle of 105°. Films were spin-cast at 3000 2π rad min^{-1} with 21400 2π rad min^{-1} s^{-1} (for the SP film) or 400 2π rad min^{-1} s^{-1} (for the TCB film) acceleration. After spin-casting, films were heated to 180 °C for 10 min and then cooled at ca. 5 °C min^{-1} to room temperature. These films were used directly for AFM measurement. For TEM specimen preparation, a drop of poly(acrylic acid) (PAA) aqueous solution (20% by mass) was placed onto an annealed film, cured overnight at 55 °C. The solidified PAA pellet, along with the part of film underneath, was detached from the substrate. The specimen was picked up by a blank copper grid after PAA was dissolved by floating the pellet on water for ~3 h. The retrieved film was washed repetitively by touching the back side of the copper grid to clean drops of water and then to a filter paper edge. For preparing transistors, all the processing parameters were kept constant with those descibed above, except that native oxides of <100> silicon were replaced by bottom-contact test beds with degenerately doped n^+ silicon wafers as gates and thermally grown SiO_2 (200 nm thick) as the gate dielectric. The source and drain electrodes with fixed channel width (1 mm) and variable channel lengths were deposited by e-beam evaporation with 5 nm of titanium and 40 nm of gold and patterned by photolithography and a lift-off process.

Characterization: A Philips EM400T transmission electron microscope, operated at 120 kV, was used to perform imaging and electron diffraction. The images were recorded with an SIS Cantega 2 K CCD camera. AFM was performed on a Digital Instruments Nanoscope IV in tapping mode. *I–V* characteristics were measured in a vacuum cryogenic probe station.

Image Analysis: Igor Pro (version 5.05) was used to process and analyze all the images. Local histogram-equalization and 2D power spectrum calculation were performed by using built-in functions. Pixel-by-pixel analysis, circular averaging of the 2D power spectra, and neighborhood analysis were performed by using customized programs.

Supporting Information

Supporting Information is available from the Wiley Online Library or from the author.

Acknowledgements

Merck Chemicals (UK) is gratefully acknowledged for providing the semiconducting polymer. The authors thank Dr. L. J. Richter, Dr. R. J. Kline, Dr. C. L. Soles, and Prof. D. C. Martin for useful discussions. X. Z. thanks Dr. C. Chan for fabricating bottom-contact transistor test beds. This official contribution of the National Institute of Standards and Technology is not subject to copyright in the United States.

Received: June 17, 2010
Published online: September 23, 2010

[1] V. Coropceanu, J. Cornil, D. A. da Silva Filho, Y. Olivier, R. Silbey, J.-L. Brédas, *Chem. Rev.* **2007**, *107*, 926.
[2] a) M. L. Chabinyc, A. Salleo, *Chem. Mater.* **2004**, *16*, 4509; b) G. Horowitz, *J. Mater. Res.* **2004**, *19*, 1946; c) P. W. M. Blom, V. D. Mihailatchi, L. J. A. Koster, D. E. Markov, *Adv. Mater.* **2007**, *19*, 1551; d) Y.-L. Loo, I. McCulloch, *MRS Bull.* **2008**, *33*, 653.
[3] R. A. Street, J. E. Northrup, A. Salleo, *Phys. Rev. B* **2005**, *71*, 165202.
[4] a) C. C. Mattheus, A. B. Dros, J. Baas, G. T. Oostergetel, A. Meetsma, J. L. de Boer, T. T. M. Palstra, *Synth. Met.* **2003**, *138*, 475; b) S. E. Fritz, S. M. Martin, C. D. Frisbie, M. D. Ward, M. F. Toney, *J. Am. Chem. Soc.* **2004**, *126*, 4084; c) R. Ruiz, D. Choudhary, B. Nickel, T. Toccoli, K.-C. Chang, A. C. Mayer, P. Clancy, J. M. Blakely, R. L. Headrick, S. Iannotta, G. G. Malliaras, *Chem. Mater.* **2004**, *16*, 4497; d) R. Ruiz, A. Papadimitratos, A. C. Mayer, G. G. Malliaras, *Adv. Mater.* **2005**, *17*, 1795; e) M. Kitamura, Y. Arakawa, *J. Phys.: Condens. Matter* **2008**, *20*, 184011.

[5] a) Z. Bao, A. Dodabalapur, A. J. Lovinger, *Appl. Phys. Lett.* **1996**, *69*, 4108; b) H. Sirringhaus, P. J. Brown, R. H. Friend, M. M. Nielsen, K. Bechgaard, B. M. W. Langeveld-Voss, A. J. H. Spiering, R. A. J. Janssen, E. W. Meijer, P. Herwig, D. M. de Leeuw, *Nature* **1999**, *401*, 685; c) B. Grévin, P. Rannou, R. Payerne, A. Pron, J.-P. Travers, *Adv. Mater.* **2003**, *15*, 881; d) D. M. DeLongchamp, B. M. Vogel, Y. Jung, M. C. Gurau, C. A. Richter, O. A. Kirillov, J. Obrzut, D. A. Fischer, S. Sambasivan, L. J. Richter, E. K. Lin, *Chem. Mater.* **2005**, *17*, 5610; e) R. J. Kline, M. D. McGehee, E. N. Kadnikova, J. Liu, J. M. J. Fréchet, M. F. Toney, *Macromol.* **2005**, *38*, 3312.

[6] a) G. Horowitz, M. E. Hajlaoui, *Adv. Mater.* **2000**, *12*, 1046; b) Horowitz, M. E. Hajlaoui, *Synth. Met.* **2001**, *122*, 185; c) A. Di Carlo, F. Piacenza, A. Bolognesi, B. Stadlober, H. Maresch, *Appl. Phys. Lett.* **2005**, *86*, 263501; d) S. S. Lee, C. S. Kim, E. D. Gomez, B. Purushothuman, M. F. Toney, C. Wang, A. Hexemer, J. E. Anthony, Y.-L. Loo, *Adv. Mater.* **2009**, *21*, 3605; e) L. H. Jimison, M. F. Toney, I. McCulloch, M. Heeney, A. Salleo, *Adv. Mater.* **2009**, *21*, 1568.

[7] a) K. Puntambekar, J. Dong, G. Haugstad, C. D. Frisbie, *Adv. Funct. Mater.* **2006**, *16*, 879; b) V. Kalihari, E. B. Tadmor, G. Haugstad, C. D. Frisbie, *Adv. Mater.* **2008**, *20*, 1.

[8] a) I. McCulloch, M. Heeney, C. Bailey, K. Genevicius, I. McDonald, M. Shkunov, D. Sparrowe, S. Tierney, R. Wagner, W. Zhang, M. L. Chabinyc, R. J. Kline, M. D. McGehee, M. F. Toney, *Nat. Mater.* **2006**, *5*, 328; b) D. M. DeLongchamp, R. J. Kline, E. K. Lin, D. A. Fischer, L. J. Richter, L. A. Lucas, M. Heeney, I. McCulloch, J. E. Northrup, *Adv. Mater.* **2007**, *19*, 833; c) B. H. Hamadani, D. J. Gundlach, I. McCulloch, M. Heeney, *Appl. Phys. Lett.* **2007**, *91*, 243512; d) R. J. Kline, D. M. DeLongchamp, D. A. Fischer, E. K. Lin, M. Heeney, I. McCulloch, M. F. Toney, *Appl. Phys. Lett.* **2007**, *90*, 062117; e) D. M. DeLongchamp, R. J. Kline, Y. Jung, E. K. Lin, D. A. Fischer, D. J. Gundlach, S. K. Cotts, A. J. Moad, L. J. Richter, M. F. Toney, M. Heeney, I. McCulloch, *Macromolecules* **2008**, *41*, 5709; f) M. L. Chabinyc, M. F. Toney, R. J. Kline, I. McCulloch, M. Heeney, *J. Am. Chem. Soc.* **2007**, *129*, 3226; g) D. M. DeLongchamp, R. J. Kline, Y. Jung, D. S. Germack, E. K. Lin, A. J. Moad, L. J. Richter, M. F. Toney, M. Heeney, I. McCulloch, *ACS Nano* **2009**, *3*, 780.

[9] D. B. Williams, C. B. Carter, in *Transmission Electron Microscopy*, Vol. *1*, Plenum Press, New York **1996**, Ch. 9.

[10] E. S. Sherman, W. W. Adams, E. L. Thomas, *J. Mater. Sci.* **1981**, *16*, 1.

[11] J. Petermann, H. Moritz, U. Rieck, B. A. Wood, E. L. Thomas, *J. Mater. Sci.* **1989**, *8*, 1023.

[12] S. Kumar, W. W. Adams, *Polymer* **1990**, *31*, 15.

[13] L. Reimer, *Transmission Electron Microscopy: Physics of Image Formation and Microanalysis*, Springer-Verlag, Berlin **1993**.

[14] S. Chandrasekhar, *Liquid Crystals*, University Press, Cambridge **1977**.

[15] a) C. Kübel, L. González_Ronda, L. F. Drummy, D. C. Martin, *J. Phys. Org. Chem.* **2000**, *13*, 816; b) L. González_Ronda, D. C. Martin, *Macromol.* **2004**, *37*, 2872.

[16] a) A. M. Donald, A. H. Windle, *J. Mater. Sci.* **1983**, *18*, 1143; b) E. L. Thomas, B. A. Wood, *Faraday. Discuss. Chem. Soc.* **1985**, *79*, 229; c) B. A. Wood, E. L. Thomas, *Nature* **1986**, *324*, 655; d) S. D. Hudson, E. L. Thomas, *Phys. Rev. Lett.* **1989**, *62*, 1993; e) S. D. Hudson, E. L. Thomas, *Phys. Rev. A* **1991**, *44*, 8128.

[17] S. Tierney, I. McCulloch, *Synth. Met.* **2005**, *148*, 195.

[18] NIST disclaimer: Certain commercial equipment, instruments or materials are identified in this paper in order to adequately specify the experimental details. Such identification does not imply recommendation or endorsement by the National Institute of Standards and Technology nor does it imply the materials or equipment identified are necessarily the best available for this purpose.